

# The Optical Autocovariance Wind Lidar. Part I: OAWL Instrument Development and Demonstration

SARA C. TUCKER AND CARL S. WEIMER

*Ball Aerospace, Boulder, Colorado*

SUNIL BAIDAR AND R. MICHAEL HARDESTY

*Cooperative Institute for Research in Environmental Sciences, University of Colorado Boulder,  
and NOAA/Earth System Research Laboratory/Chemical Sciences Division, Boulder, Colorado*

(Manuscript received 19 February 2018, in final form 23 August 2018)

## ABSTRACT

We present the motivation, instrument concept, hardware descriptions, and initial validation testing for a Doppler wind lidar (DWL) system that uses optical autocovariance (OA) in a field-widened quadrature Mach–Zehnder interferometer lidar to measure Doppler shifts from atmospheric-aerosol-backscattered laser light. We describe system architectures for three different generations of the direct-detection aerosol Optical Autocovariance Wind Lidar (OAWL) system, including the current two-line-of-sight, dual-wavelength (355 and 532 nm) airborne configuration, designed to be an airborne demonstrator for potential space-based global wind measurement applications. We provide meter-per-second-precision results from a ground-based 355-nm OAWL aerosol winds measurement validation study alongside another DWL, results from an autumn 2011 airborne validation testing performed with radar wind profiler data, and wind measurement results from airborne validation flight testing using the 532-nm wavelength in spring 2016.


## 1. Background on OA: Motivation for a new wind lidar

Wind observations are critical inputs to weather and air quality forecast models. Observations within the existing global winds network with the highest impact on numerical weather prediction, however, are limited to profiles overland (e.g., aircraft-based sensors, radiosonde profiles), the near-surface layer (e.g., sea surface winds), or limited-layer measurements (e.g., atmospheric motion vector winds and aircraft sensors over the ocean). Vertically resolved wind profile measurements are consistently listed as one of the largest observation data gaps [e.g., World Meteorological Organization (WMO) OSCAR database; <https://www.wmo-sat.info/oscar/>], a gap particularly pronounced over the oceans and the Southern Hemisphere (Baker et al. 2014). Alternative satellite remote sensing measurements are needed to fill this gap.

Doppler wind lidars (DWLs) remotely measure range-resolved wind speeds projected onto the instrument pointing line of sight (LOS) by sending out laser light and measuring changes in frequency (Doppler shifts) in the light backscattered off the atmosphere. The DWL field has grown quickly in recent years, driven by the demand for improved and increasingly localized wind measurements and weather forecasts (e.g., for the renewable energy sector) and by the availability of reliable laser sources, electronics, and optics, including fiber optics and laser optic coatings (Boquet et al. 2016). As commercial ground-based wind lidar systems become more readily available, the use and understanding of DWL systems and the integration of the wind products increases.

Meanwhile, the need remains for space-based wind lidars capable of filling gaps in global coverage of tropospheric and lower-stratospheric wind profiles. This is despite observing system simulation experiment (OSSE) results demonstrating that space-based wind lidar would have a significant impact on weather and air quality forecast skill by increasing wind observations in numerical weather prediction (NWP)

---

 Denotes content that is immediately available upon publication as open access.

---

Corresponding author: Sara C. Tucker, [stucker@ball.com](mailto:stucker@ball.com)

models (Stoffelen et al. 2006; Marseille et al. 2008; Baker et al. 2014; Atlas et al. 2015).

#### *a. Space-based wind lidar developments*

The European Space Agency (ESA) developed the Aeolus DWL mission, successfully launched on 22 August 2018, to demonstrate the impact that operational wind lidars would have on the wind measurement gap (Endemann 2006; Clissold 2008; Reitebuch et al. 2009; Paffrath et al. 2009; Le Rille et al. 2012; Straume et al. 2016; ESA 2018). The single-line-of-sight (LOS) Atmospheric Laser Doppler Instrument (ALADIN) on Aeolus uses a 355-nm laser to measure winds using Doppler-shifted lidar returns backscattered from both atmospheric aerosols (particulates, including cloud droplets) and molecules. The aerosol (Mie scattering) channel uses Fizeau interferometer fringe imaging to measure winds using scattered returns from particulates, while the molecular (Rayleigh scattering) channel uses a double-edge Fabry–Perot etalon (Reitebuch 2012; Korb et al. 1997; Flesia et al. 2000) to measure winds in low/no-aerosol regions of the troposphere and lower stratosphere.

Implementation of a space-based wind lidar mission in the United States, however, has faced multiple challenges over the last few decades in areas such as technology readiness, reliability, cost, and political priorities. To address some of these challenges, Ball Aerospace (Ball), with additional support from NASA's Earth Science Technology Office, has invested in the build and demonstration of the Optical Autocovariance (OA) Wind Lidar (OAWL; Grund et al. 2009; Tucker et al. 2016b), which promises cost savings for future wind missions by providing options for measuring winds from aerosol and molecular returns; removing laser frequency stability requirements, using a field-widened interferometer; and building on direct-detection lidar system components like those used on Aeolus and the CALIPSO lidar (Hunt et al. 2009; Winker et al. 2009).

#### *b. OA and Mach–Zehnder Doppler lidar*

The term “optical autocovariance” describes the operation that takes place in interferometers, such as the simple moving-arm Michelson: a beamsplitter creates two copies of the illumination and one copy is time delayed (lagged) relative to the other via differences in the optical pathlengths. Upon recombination of the two optical signals at the square-law detector, the intensity corresponds to the optical autocovariance function (OACF) of the complex field functions for the given lag. Light from narrowband laser sources that exhibit a high degree of temporal coherence (a long coherence length) relative to the total optical path difference (OPD) results in higher constructive and destructive interference levels (e.g.,

higher fringe contrast visibility) than relatively short-coherence-length broadband light. Instead of a moving arm, lags can be introduced as phase delays using reflections, phase plates, and/or wave plates.

Referencing the optical autocovariance concept described in Schwiesow and Lading (1981), Schwiesow and Mayor (1995) first presented the idea of using a modified Michelson interferometer to directly measure the OACF of backscattered lidar returns for Doppler wind measurements. They suggested introducing lags using either mirrors with three stepped phases or a quarter-wave plate (QWP), resulting in four  $\lambda/4$ -stepped (quadrature) phase detection, where  $\lambda$  is the wavelength. Liu and Kobayashi (1996) presented a similar stepped phase idea with design concepts for two-channel and four-channel discriminator systems based on a Mach–Zehnder interferometer (MZI) but did not demonstrate the measurement technique. Bruneau (2001) presented two- and four-channel MZI designs for a molecular wind lidar, and Bruneau and Pelon (2003) further expanded on the use of MZI for the study of aerosol backscatter and extinction with winds. Their paper contains an excellent overview of MZI Doppler measurements. Bruneau et al. (2004) presented the first published measurements of winds using a short (5 cm) OPD MZI to resolve Doppler-broadened molecular-backscattered winds up to 40-km altitude. More recently this group demonstrated 29.4- and 20-cm OPD instruments for winds and aerosol studies (Bruneau et al. 2013, 2015). MZI systems can also incorporate planar detector arrays to resolve fringe shifts; such fringe imaging designs have been presented by Bruneau (2002) and Herbst and Vrancken (2016).

Ball Aerospace began development of OAWL system hardware in 2004. The first proof of concept system, demonstrated in a laboratory setting and validated using a sonic anemometer in 2006, used a three-phase, stepped-coating window (Grund et al. 2008). In 2007, the team designed a cat's-eye field-widened, reflective, multiwavelength, quadrature Mach–Zehnder interferometer (QMZI) receiver (Grund et al. 2009). Patents were awarded for the method and apparatus in 2011 (Grund and Pierce 2009a,b). Development, design, and build efforts through 2009 culminated in a prototype QMZI with a 90-cm OPD. Additional information on the OAWL interferometer and how it compares to other QMZIs used for DWL measurements is provided in section 2c(4). This paper focuses on the instrument design, implementation, and demonstration of the QMZI approach in OAWL.

#### OAWL OPERATION

The OAWL measurement operation uses a QMZI to measure the OACF at four points (separated by  $\lambda/4$ ) to determine the phase and visibility of fringes produced by

laser illumination of wavelength  $\lambda$ , and to measure the relative changes in that phase between outgoing pulses of laser light and the backscattered Doppler-shifted lidar returns on a pulse-by-pulse basis. In OAWL operation, a small sample of the outgoing laser pulse is captured and used to probe the instantaneous laser-frequency-and-interferometer-dependent fringe phase at time 0 (T0; blue dots in Fig. 1). The four detector samples are used to find the T0 fringe phase offset relative to the defined detector phases ( $0, \pi/2, \pi$ , and  $3\pi/2$ ) following a sinusoid phase estimation algorithm like that defined in [Browning and Wexler \(1968\)](#) for velocity–azimuth display (VAD)-based retrievals. When applicable, lidar platform (e.g., aircraft or spacecraft) motion may be projected onto the lidar LOS ([Hill et al. 2008](#)), translated into a phase shift  $\phi_{\text{platform}}$  by inverting Eq. (3), and then added to  $\phi_{T0}$  to account for platform-induced Doppler shifts on a per-pulse basis prior to accumulation. Each pulse's T0 phase offset  $\phi_{T0}$  is used to adjust the detector phase definitions ( $0 + \phi_{T0}, \pi/2 + \phi_{T0}, \pi + \phi_{T0}$ , and  $3\pi/2 + \phi_{T0}$ ) for all lidar return samples, for that pulse (red diamonds in Fig. 1). The lidar returns are accumulated over the desired number of range samples and laser pulses before performing a sinusoidal fit and retrieving the Doppler-shifted return signal phase  $\Delta\phi$  for that range gate. Because the phase shifts in the lidar returns are all referenced to the outgoing phase for each laser pulse, the system is described as “self-referencing.” This process allows for pulse-to-pulse variations in the interferometer OPD, the laser pulse frequency, and/or the platform-induced Doppler shifts, without signal degradation. Accumulating the phase-shifted detector values prior to fitting the sinusoid improves the sinusoid signal-to-noise ratio and thus the precision of the fit by a factor of  $\sim\sqrt{N_p}$ , where  $N_p$  is the number of pulses, limited by atmospheric variability over the accumulation time. Phase changes from laser frequency or platform- or wind-induced Doppler shifts that exceed the free spectral range (FSR) of the interferometer will wrap around (like aliasing), resulting in removable  $2\pi$  phase jumps; thus, the reference and return phases are always captured. Fringe wrapping eliminates the need to tightly control the laser frequency or the interferometer pathlength and avoids “out of band” signal loss observed with some types of DWLs. Phase changes caused by small vibration-induced pulse-to-pulse variations in OPD are also captured and unwrapped; however, the cat’s-eye system generally stays aligned to within  $\ll 1$  mm of the OPD design point to avoid defocus that would reduce the interferometer contrast.

The Doppler-shifted frequency change in atmospheric-backscattered laser light is related to the laser wavelength  $\lambda_0$  (frequency  $f_0$ ) and the wind speed projected onto the lidar LOS  $v_{\text{LOS}}$  via

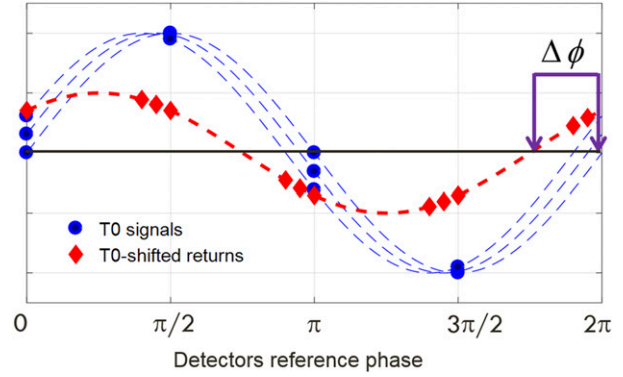


FIG. 1. Example fringe intensities at the four OAWL interferometer detector points from the outgoing laser illumination (blue) and corresponding Doppler-shifted (red) returns for a single range gate. Detectors are defined for constant reference phase, with  $\pi/4$  separation. Sinusoidal fits to multiple sets (representing multiple laser pulses) of T0 detector values (blue circles) determine the relative reference phase  $\phi_{T0}$  for each pulse, used to shift the detector phase definitions for all corresponding lidar returns for that pulse. Doppler-shifted return signals are built up by accumulating T0 phase-shifted samples (sets of red diamonds) from multiple pulses prior to estimating the self-referenced, wind-induced phase offset  $\Delta\phi$  for that gate and then translated into wind speed using Eq. (1).

$$\Delta f_D = 2 \frac{v_{\text{LOS}}}{c} f_0 = \frac{2v_{\text{LOS}}}{\lambda_0}. \quad (1)$$

The resulting change in interferometer fringe phase ( $\Delta\phi$ , rad) is determined by the ratio of  $\Delta f_D$  to the interferometer FSR. Here,  $\text{FSR} = c/\text{OPD}$ , where OPD is twice the difference in the interferometer arm lengths and  $c$  is the speed of light. The interferometric phase shift caused by the wind-induced Doppler shift, in fractions of  $2\pi$  radians, is given by

$$\frac{\Delta\phi}{2\pi} = \frac{\Delta f_D}{\text{FSR}} = \frac{\Delta f_D \text{OPD}}{c}, \quad (2)$$

and the LOS wind speed estimate is

$$v_{\text{LOS}} = \frac{\lambda \Delta f_D}{2} = \frac{\lambda c}{4\pi \text{OPD}} \Delta\phi. \quad (3)$$

Based on the Cramer–Rao lower bound for estimating the phase  $\Delta\phi$  of a sinusoid assuming  $N$  samples in the fit, the precision is given for large  $N$  by ([Kay 1993](#))

$$\sigma_{\Delta\phi}(N) \geq \frac{\sqrt{2}}{\text{CNR}\sqrt{N}}, \quad (4)$$

where the Doppler-shifted carrier-signal-to-noise ratio (CNR) is a function of the direct-detection lidar signal-to-noise-ratio (SNR) and the interferometer measurement contrast visibility  $V_m$ :

$$\text{CNR} = V_m \text{SNR}. \quad (5)$$

SNR is a function of lidar radiometry (laser power, telescope aperture, range, instrument throughput efficiency, and total aerosol and molecular atmospheric scattering), and  $V_m$  is a function of interferometer alignment, laser coherence length relative to the interferometer OPD, and the aerosol-to-molecular scattering ratio of the backscattered return (see [section 2a](#); [Bruneau and Pelon 2003](#)).

Combining Eqs. (3) and (4) provides the minimum precision for the OAWL LOS wind measurement  $\sigma_{v_{\text{LOS}}}$ :

$$\sigma_{v_{\text{LOS}}}(N) = \frac{\lambda c}{4\pi \text{OPD}} \sigma_{\Delta\phi}(N) \geq \frac{\lambda c}{4\pi \text{OPD}} \frac{\sqrt{2}}{\text{CNR}\sqrt{N}}. \quad (6)$$

Additional discussion on OAWL theoretical performance, error analysis, and comparison to work done on MZI precision in [Bruneau and Pelon \(2003\)](#) is out of the scope of this instrument-build paper, but it will be provided in an upcoming paper.

### c. OAWL evolution

The OAWL system evolution has specifically been directed toward space-based operation. Building a new observation instrument for space requires raising the instrument technology readiness levels (TRLs; [NASA 2007](#)) through development, demonstration, environmental testing, and often, as in the case for ESA's Aeolus, through airborne demonstrations ([Durand et al. 2004](#); [Reitebuch et al. 2009](#), [Marksteiner et al. 2011](#), [Lux et al. 2018](#)). To this end, the OAWL lidar system evolved from an initial laboratory demonstration, through a single-wavelength (355 nm), single-LOS, prototype breadboard system ([Grund and Tucker 2011](#)), to a dual-wavelength, dual-look (two telescopes with separate LOSs), airborne demonstrator for space-based mission concepts ([Tucker et al. 2016a](#); [Baidar et al. 2016](#)).

The 355-nm single-LOS OAWL prototype instrument (OAWL-P) build started in 2008, with ground and flight test demonstrations in 2011. Adding 532-nm-wavelength channels in 2013 enabled demonstration of dual-wavelength wind measurements that inform wavelength trade studies for space-based operation. The 355-nm ultraviolet wavelength (chosen by ESA for Aeolus) provides higher molecular scattering and additional aerosol scattering but mitigation strategies must be implemented to reduce the risk of laser damage in space-based operation. In contrast, the 532-nm wavelength poses less laser damage risk but sees increased solar background, greater restrictions on minimum divergence to meet eye safety requirements, and smaller lidar backscatter (aerosol and molecular) than the 355-nm wavelength.

Both the 355- and 532-nm wavelengths can be generated from 1064-nm neodymium-doped yttrium aluminum garnet (Nd:YAG) lasers like those used on *CALIPSO*. While the CALIOP laser is not injection seeded, the *CALIPSO* instrument has demonstrated the 532-nm wavelength from space at  $\sim 100$  mJ per pulse for over 12 years in orbit. The Aeolus mission has space-qualified injection-seeded 355-nm Nd:YAG lasers ([ESA 2017](#)), and the injection-seeded high-efficiency ultraviolet demonstrator laser, (HEUVD; [Albert et al. 2016](#)), currently undergoing lifetime testing at Fibertek, Inc., operates at both 532- and 355-nm wavelengths.

For space-based operations, laser readiness is key to containing mission risk and thus mission cost. Demonstrating OAWL at the 532-nm wavelength formed the basis of the Atmospheric Transport, Hurricanes, and Extratropical Numerical Weather Prediction Using OAWL (ATHENA-OAWL) mission concepts proposed for NASA Earth Venture Instrument (EVI) opportunities in 2013 and 2016. The mission was originally proposed for operation from the International Space Station to keep within the EVI cost constraints. In contrast, investments in ESA's free-flyer, space-based wind lidar Aeolus mission are significantly larger, enabling the use of injection-seeded 355-nm lasers by mitigating UV damage ([Straume et al. 2016](#)). Additional information about the ATHENA-OAWL mission concept may be found in [Tucker et al. \(2016b\)](#).

NASA rated the ATHENA-OAWL EVI-2013 proposal a category 3 ("key technologies too high of risk for mission"), but because of the high scientific and technological impact of the potential mission, they awarded Venture Technology Development ("Venture-Tech") funding to build, demonstrate, and validate a 532-nm-wavelength airborne demonstrator lidar system, Green OAWL (GrOAWL), with two independent looks (lines of sight) to enable wind speed and direction profile retrievals. Recent development efforts added the 355-nm-wavelength and cross-polarization measurements to the two-look GrOAWL system for dual-wavelength winds and high-spectral-resolution lidar (HSRL) measurements. The resulting upgraded instrument is called HSRL for Aerosols, Winds, and Clouds Using OAWL (HAWC-OAWL).

## 2. Hardware evolution

To illustrate and highlight trade-offs encountered in the OAWL system development, this section describes the evolution of the various instrument subsystems as they were matured for eventual space application. The all-aluminum MZI sits at the heart of all the OAWL configurations designed, built, and demonstrated between 2008 and 2017. Each system has also included, at



minimum, aircraft support hardware, optical bench, laser(s), telescope(s), laser fluid cooling loop(s), thermal control systems, and payload controller with software and data acquisition systems (see Fig. 2). Images of the different systems, described in the following subsection, are provided in Fig. 3.

#### a. Design considerations

Lidar return signal strength scales linearly with laser power and receiver efficiency (including detector quantum efficiency) and quadratically with telescope diameter. For the OAWL configurations described here, design parameters were based on the best available hardware for the given cost, mass, and volume restrictions. The choice to use Nd:YAG lasers is based on *CALIPSO* space heritage and the larger atmospheric aerosol lidar backscatter coefficients observed at shorter wavelengths (relative to, for example, near-IR wavelengths).

The interferometer OPD is chosen based on the atmospheric application (Grund et al. 2008). The performance of the OAWL system is a function of the measurement visibility  $V_m$  (or contrast) of the fringe in the interferometer, which is a function of the line shape of the illumination; the coherence length  $L_c$ , which is a function of the spectral bandwidth; and the interferometer OPD. For a Gaussian laser line shape, the fringe contrast is approximated as (Goodman 1985, 165–168)

$$V_m = V_{\max} \exp \left[ -\pi \left( \frac{\text{OPD}}{L_c} \right)^2 \right], \quad (7)$$

where  $V_{\max}$ , a function of interferometer optical quality, wavelength, and alignment, varies between 0.8 and 0.95 depending on the interferometer optics and alignment status. Doppler-broadened molecular backscatter has a wide bandwidth and thus a short coherence length (a few centimeters), while aerosol backscatter has approximately the same coherence length as the transmitted laser pulse ( $\sim 6$  m for the OAWL lasers, resulting in a maximum  $V_m$  of  $\sim 0.74$ ). While long OPD systems can resolve fringes from the narrowband aerosol-backscattered returns, the wide-band molecular returns will be unresolved, adding only an offset. Thus, the 90-cm OPD interferometer wind measurement precision is optimal when aerosol loading is high. The long OPD also separates aerosol (fringe) and molecular (offset) components of the return to simultaneously measure winds and aerosol scattering ratio profiles by the HSRL method as described in Grund et al. (2009). Alternatively, short OPD (e.g., 3–5 cm) interferometers can resolve fringes using the short-coherence-length illumination observed from Doppler-broadened molecular-backscattered lidar returns (Bruneau et al. 2004; Grund et al. 2009). Thus, short

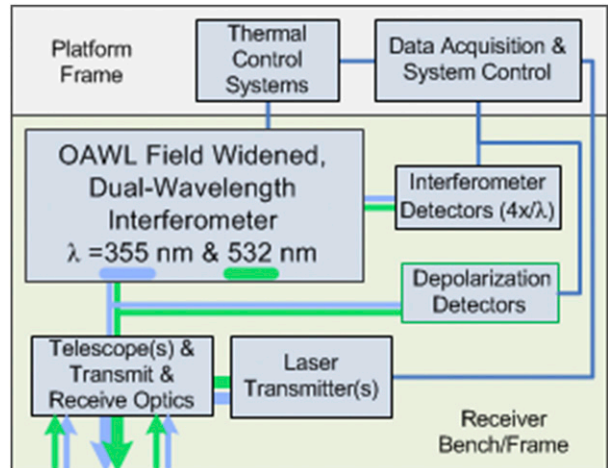


FIG. 2. Generic OAWL instrument system block diagram.

OPD QMZI systems measure winds under any aerosol loading conditions (including no aerosols), but the per-sample uncertainty will be higher because of the shorter OPD [see Eq. (6)] and larger FSR. An OAWL interferometer system is currently under development at Ball that implements a short OPD to measure winds using the 355-nm returns backscattered from both molecules and aerosols. The OAWL systems described in this paper, however, used the same 90-cm OPD interferometer to demonstrate high-precision direct-detection measurement of aerosol winds using the 355- and 532-nm wavelengths.

#### b. Optomechanical architecture

The OAWL instrument architectures are driven by the lidar science requirements, program objectives, and the platform constraints. Figure 2 contains the basic block-diagram architecture common to the different evolutions of the OAWL instrument. Table 1 lists the major system parameters for the OAWL-P, GrOAWL, and HAWC-OAWL airborne lidar systems. Both OAWL-P and GrOAWL flew on the NASA WB-57 jet inside the partially pressurized (up to 34.5 kPa above ambient) pallet; however, their layouts were significantly different. HAWC-OAWL, derived largely from GrOAWL, is configured for future flights on the NASA DC-8 aircraft.

The OAWL-P effort sought to provide a preliminary demonstration of the optical autocovariance approach to measuring winds, and the program afforded only building a prototype instrument, largely using commercial off-the-shelf (COTS) parts. The OAWL-P optical bench consisted of a master oscillator power amplifier (MOPA) Fibertek laser transmitter, a telescope, an OA interferometer, detectors, and interim transmit–receive optics,

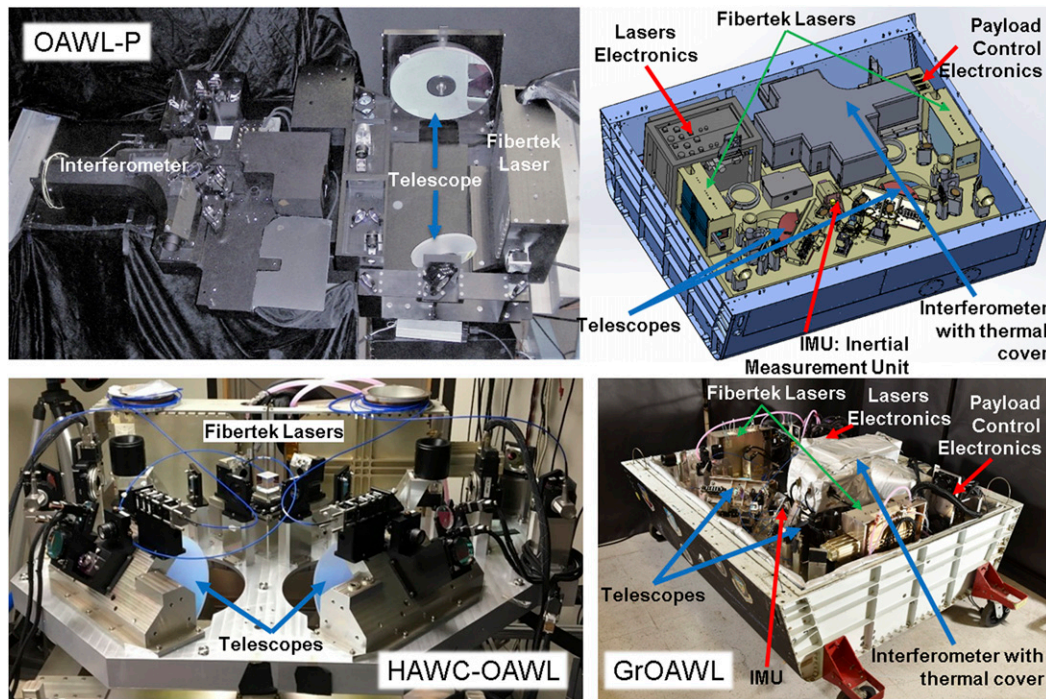


FIG. 3. (top left) OAWL-P breadboard prototype system, (top right) model of the 2016 GrOAWL system inside the NASA WB-57 pallet base, (bottom right) GrOAWL system installed inside the pallet, and (bottom left) HAWC-OAWL transmit-receive optical bench configured for the NASA DC-8.

mounted and aligned in one plane on a  $\sim 15$ -cm-thick honeycomb breadboard optical bench. For ground test operations, the breadboard mounted to a rotatable bench provided adjustable elevation pointing angles to point through exterior windows or doors at ground test sites. For airborne testing, the breadboard was installed at a  $45^\circ$  angle inside the WB-57 pallet. While 355-nm scanner technology has been demonstrated (Schwemmer et al. 2001, 2006), scanning imposes a high cost, so the OAWL-P system had only a single static-pointing look and used the aircraft to scan for the flight demonstration. The single-LOS beam pointed out of the aircraft as shown in Fig. 4 (blue lines). Additional information about the 2011 aircraft installation is provided in Tucker et al. (2015).

In contrast, the 532-nm GrOAWL effort sought to demonstrate the proposed space-based, two-look measurement geometry, to validate the measurement approach, and to develop the technology readiness of the subsystems for space. The GrOAWL system was considered an airborne demonstrator for future space-based missions, so components that have a path to space or space equivalent were used wherever possible in the design. The system also included specialized aircraft hardware, vibration isolation, and heating and cooling systems to handle the wide range of temperature, pressure, and relative humidity variations and

high vibration levels unique to the harsh WB-57 aircraft environment.

GrOAWL, (now HAWC-OAWL) uses two Fibertek Nd:YAG lasers to transmit (with interleaved pulses) and two Cassegrain telescopes to receive. The two telescope receiver paths are combined into the QMZI receiver using a polarizing beamsplitter (PBS); no mechanical switching is required. To provide independent measurements of the winds, the looks were separated azimuthally by  $90^\circ$ , with look 1 pointed at  $45^\circ$  (“forward” look) and look 2 at  $135^\circ$  (“aft” look) azimuth, relative to aircraft forward. Both looks are then rotated down  $45^\circ$  from horizontal (see Fig. 4, green lines). This architecture reflects the two-telescope approach proposed for some space-based wind lidar missions, including ATHENA-OAWL (Weimer et al. 2015; Tucker et al. 2016b). While the configuration provides measurements of two components of the wind field that may be combined to retrieve horizontal speed and direction profiles, NWP would assimilate the looks separately (Ma et al. 2015). As the lidar platform (aircraft or spacecraft) flies along a flight track, the aft look measures winds along approximately the same narrow volume as the forward look, but with time delays that depend on platform speed and range to the atmospheric volume. To the authors’ knowledge, GrOAWL was the

TABLE 1. OAWL system parameters. IMU = inertial motion unit.

Parameter	OAWL-P	GrOAWL 2016	HAWC-OAWL
Laser 1 name	OAWL-1	Refurbished OAWL-1	Refurbished OAWL-1
Laser 2 name	Not applicable	GrOAWL	GrOAWL
Laser wavelength(s)—Nd:YAG fundamental wavelength: 1064 nm	355 nm	532 nm	532 and 355 nm (from same Nd:YAG lasers)
Pulse repetition rate	200 Hz	200 Hz per laser = 400 Hz for data system	
Operational laser pulse energies	20 mJ	Variable: 200 $\mu$ J–2.5 mJ	532 nm: up to 2.5 mJ 355 nm: up to 20 mJ
Laser pulse length	$\sim$ 18 ns		$\sim$ 22–26 ns
Laser pulse bandwidth	$\sim$ 42 MHz	$\sim$ 30 MHz	532 nm: 32 MHz 355 nm: 33 MHz
Interferometer		Aluminum structure interferometer with 90-cm OPD	
Interferometer unambiguous LOS velocity range [Eq. (3) scaled by $\pm\pi$ ]		532 nm: $\pm 44.3 \text{ ms}^{-1}$ 355 nm: $\pm 29.6 \text{ ms}^{-1}$	
Number of lasers/telescopes/looks	1	2	2 (dual wavelength)
Telescope effective aperture diameter(s) (including obscurations)	25 cm	28 cm	29 cm
Detector channels: Hamamatsu MPPC (model number)	Interferometer: Four at 355 nm (s10362–025)	Interferometer: Four at 532 nm (s12571–025)	Interferometer: Four at 355 nm and four at 532 nm Cross-polarization: One at 355 nm and one at 532 nm (s12571–025)
Detector quantum efficiency	0.23	0.32	532 nm: 0.32 355 nm: 0.26
Aircraft navigation, position, and orientation information	1-Hz aircraft-mounted GPS/IMU	Optical-bench-mounted	Applanix POS-AV V6 5-Hz GPS and 200-Hz IMU

first time the continuous two-look approach was demonstrated with a DWL from an aircraft platform.

The HAWC-OAWL system builds on the GrOAWL hardware (telescopes, lasers, transmit/receive optics) with the reintroduction of four 355-nm-wavelength interferometer channels and two atmospheric cross-polarization channels (one per wavelength, to enable measurement of aerosol properties), for a total of 10 channels.

### c. Optical subsystems

#### 1) LASER TRANSMITTER

The OAWL systems' laser transmitters are diode-pumped, injection-seeded (ramp and fire), conductively cooled, Q-switched Nd:YAG systems built by Fibertek, Inc., based on models built for other DWL and HSRL systems. The 200-Hz pulse repetition frequency (PRF) lasers generate the fundamental 1064-nm wavelength that is frequency doubled to 532 nm and tripled to 355 nm using temperature-controlled lithium triborate (LBO) crystals (Hovis et al. 2008).

The first laser, delivered in 2010, used in all generations of the system to date, is a single-amplifier system that dumps the unconverted 1064-nm wavelength inside the laser box prior to the beam going through an on-axis beam expander, which sets the 355- and 532-nm output beams at  $\sim$ 20-mm diameter with  $\sim$ 95- $\mu$ rad divergence.

The second GrOAWL laser (also used in HAWC-OAWL), delivered in 2016, is a two-amplifier version of the first OAWL laser that implements an off-axis beam expander designed to avoid a lossy central obscuration, and that dumps the unused 1064-nm illumination outside the laser box for space and thermal reasons. While the GrOAWL system transmits only 1.5–2.5 mJ of 532-nm laser output for typical operation, the airborne-demonstrated GrOAWL laser can produce over 80 mJ of 1064-nm illumination at 200 Hz (16 W), or about 60 mJ of 532-nm illumination at 200 Hz (12 W). Fibertek made minor modifications to both lasers so that the second (new) laser may be synchronized with the first (original) laser, resulting in alternating pulses from the two lasers for an effective 400-Hz PRF system operation with no more than 25  $\mu$ s of timing jitter.

#### 2) TRANSMIT AND RECEIVE OPTICS

To collect backscattered laser light, the OAWL-P receiver used a low-cost custom  $F/4$ ,  $\sim$ 30-cm diameter, parabolic reflector telescope, folded with two flats. A pinhole set the field of view (FOV) to 157  $\mu$ rad. The inexpensive design yielded a central obscuration that limited the maximum transmission value at full overlap (at  $\sim$ 7 km) to  $<68\%$ . The system transmit path implemented a manually adjustable boresight mirror behind the telescope secondary mirror.



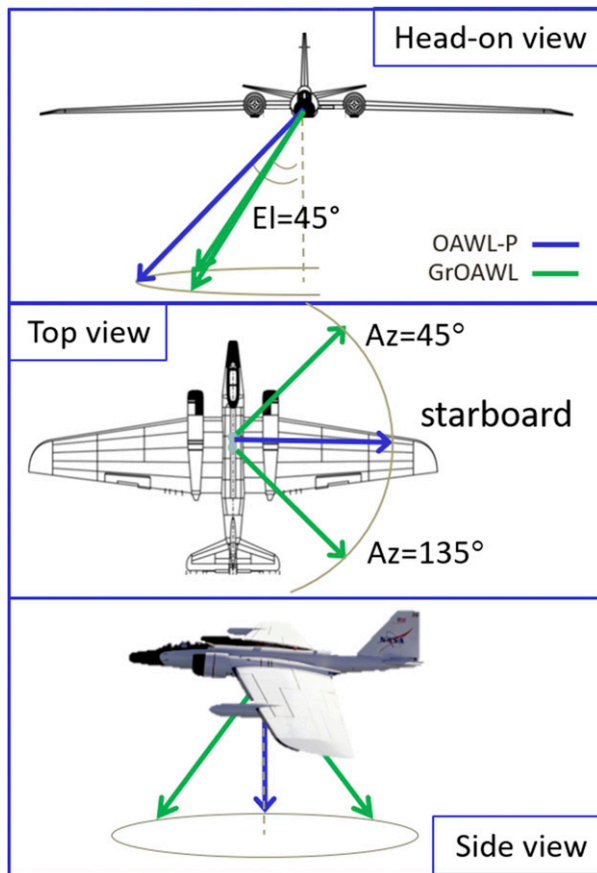


FIG. 4. Lidar beam paths from the NASA WB-57 aircraft for OAWL-P (blue lines) and GrOAWL (green lines). The 355-nm OAWL-P operated with one look pointed starboard (azimuthal angle of  $90^\circ$  from forward) and  $45^\circ$  off nadir. The 532-nm GrOAWL beams were at azimuthal angles of  $45^\circ$  (forward beam) and  $135^\circ$  (aft beam) from forward, with both beams at  $45^\circ$  off nadir [also see Fig. 1 in Baidar et al. (2018)]. Aircraft images from NASA WB-57 program office.

The GrOAWL and HAWC-OAWL systems use two  $F/8$ , 30-cm-diameter,  $200\text{-}\mu\text{rad}$  FOV, Cassegrain telescopes built by Jenoptik, with central obscurations that result in maximum overlap of  $\sim 78\%$  by  $\sim 5\text{-km}$  range. The transmit beam mirrors add some additional primary mirror obscuration. Transmit beam divergence for the two looks is between 130 and  $150\text{ }\mu\text{rad}$  depending on laser divergence and mirror and window flatness. Based on the beam size and divergence, laser eye safety requirements set the maximum amount of 532-nm laser power that can be transmitted. Each path contains a variable attenuator subsystem with a motorized rotating 532-nm half-wave plate (HWP) and polarizing beamsplitter to adjust the transmitted 532-nm laser power output with negligible effect on the 355-nm output (eye safe at much shorter ranges). Each transmit path on GrOAWL includes a remotely controlled stepper-motor boresight mechanism used to maintain overlap as needed

under the extreme thermal and window pressure variations experienced during airborne operation.

Obscuration around the final transmit mirrors block near-range single-scatter returns until overlap begins at about 400 m, thus preventing saturation of the detectors from the near-field backscatter. Returns are observed from closer ranges, however, because of atmospheric multiple scattering, particularly evident when flying through clouds.

Returns collected by the two telescopes are transferred to the interferometer using a dual-wavelength PBS. Both lasers transmit the same vertical polarization. For one receive path, backscattered laser light with polarization parallel to that of the transmit light is rotated (using a dual-wavelength HWP) before the PBS so that it will reflect into the same path as parallel polarization light from the other look.

Backscatter perpendicular to the transmit polarization is combined at the other exit of the PBS and sent to the cross-polarized return detector path, as indicated in Fig. 2, to provide information used in aerosol characterization (not discussed in this paper). If such cross-polarization information were not desired, then each telescope could be directly fiber coupled into the interferometer, allowing all returns from each telescope to be used in wind speed detection.

### 3) T0 PATH

As each laser fires, a tiny portion of the T0 pulse leaks through one of the transmit path turning mirrors and is collected into a  $150\text{-}\mu\text{m}$  core multimode fiber delay. The delay is set to  $\sim 50\text{ m}$  to avoid overlap of the T0 signal with scatter picked up by the telescope during the outgoing pulse and yet ensure T0 is measured before the telescope range overlap function begins. At the exit of the fiber, the T0 light is launched into the same path as the corresponding telescope/atmospheric return, leaking through the back of another turning mirror. Per the discussion surrounding Fig. 1, the delayed T0 pulse is used to probe the state of interferometer and laser and to determine the relative detector offset reference phases for each pulse, eliminating the need for a fixed laser wavelength. Thus, no frequency locking is required, simplifying the laser architecture.

### 4) FIELD-WIDENED INTERFEROMETER

The OAWL prototype interferometer flown on the 2011 and 2016 flight tests is the all-aluminum, cat's-eye, field-widened (Wang et al. 2000), 90-cm OPD QMZI referenced in section 1b. Field widening is particularly important for space-based lidar systems, where the following must be considered:

- 1) Large collection aperture telescopes ( $\sim 30\text{--}100\text{-cm}$  diameter) are paired with  $\sim 2\text{-cm}$  diameter (or smaller)



TABLE 2. QMZI systems built and demonstrated for DWL measurements.

	Bruneau et al. (2004)	Bruneau et al. (2013)	Bruneau et al. (2015)	Ball OAWL-P, GrOAWL, and HAWC-OAWL
Interferometer design	Monolithic (refractive)			All reflective cat's-eye
Field-widening method	Field compensation via refractive index matching			Cat's-eye design: 8 mrad FOV
Laser wavelength(s)	Nd:YAG, 532 nm	Nd:KGW, 1067 nm	Nd:YAG, 355 nm	Nd:YAG, 355 and 532 nm
OPD	5.12 cm	29.4 cm	20 cm	90 cm
Atmospheric targets	Molecular	Aerosol	Aerosol	Aerosol

frequency discriminator systems, resulting in 30–50 times (or more) magnifications of the telescope FOV, typically set to encompass the laser transmit beam divergence.

- 2) Allowing more field into the interferometer enables use of telescopes with  $\sim 1\lambda$  of wave front error, adding additional field to the return beam. The relaxed telescope requirement reduces risk and cost compared to other types of DWL systems with diffraction-limited (e.g.,  $\lambda/20$ ) telescope wave front requirements.
- 3) Multimode fibers may be used to couple light collected by telescopes to the receiver, reducing optical bench stability requirements; fiber numerical aperture, core diameter, and beam size set the minimum FOV for the interferometer.

The interferometer's cat's-eye configuration ensures that rays coming through the system with nonzero field angles have the same optical pathlengths as the chief ray when measured at the cat's-eye focal plane secondary mirror (Wang et al. 2000). From the cat's-eye focal plane to the second beamsplitter (i.e., the beam combiner), the chief and maximum field angle rays again collect different amounts of optical pathlengths; however, the same angled ray picks up the same additional path in the other arm of the interferometer, ensuring all field angles see the same differential path difference (OPD). When properly aligned, the existing interferometer is capable of handling at least 8 mrad of field (at the  $\sim 22$ -mm-diameter interferometer pupil plane) with negligible loss in fringe visibility.

In the OAWL-P system, free-space optics transferred the T0 signal and collimated telescope beams to the interferometer through a dual-wavelength HWP that rotated the vertically polarized returns to provide equal amounts of vertically and horizontally polarized light to the interferometer. Differences between the sets of field angles entering the interferometer from the T0 return path versus those from the telescope/pinhole path induced range-dependent biases in the near field of the OAWL-P system. The field angle differences varied with range (overlap function) and laser pointing. When the T0 path was properly aligned, the bias was zero at full overlap.

Observed near-field errors were verified using a two-dimensional interferometer field model, paired with an overlap-function-dependent receiver field angle model, built to characterize the overall sensitivity of the bias to range, pointing, and internal interferometer alignment errors. A full description of the model and the effects is out of the scope of this paper; however, a similar effect is thoroughly described in Herbst and Vrancken (2016).

To eliminate the overlap bias issue and to provide additional system integration flexibility, the GrOAWL system incorporates a multimode fiber that sufficiently scrambles both the field angles and the polarization. The fiber projects a uniform and consistent 3.4-mrad-wide field distribution into the interferometer for both the T0 pulses and the atmospheric return from all ranges, thus avoiding overlap-function-based variations in field. The fiber also scrambles polarization such that the distribution of horizontal and vertical polarization entering the interferometer are approximately the same (see Bruneau et al. 2013), eliminating the need for a HWP at the interferometer entrance. Any remaining differences in polarization balance are removed via regular data-based signal calibration. Speckle in the fiber-launched optical field does not impact the QMZI performance.

Table 2 lists the design parameters for the current OAWL interferometer and for systems designed and/or built by Bruneau and colleagues for comparison. The OAWL interferometer schematic, with detectors set up for the HAWC-OAWL configuration, is provided in Fig. 5 and follows the system descriptions in Grund et al. (2009). A dual-wavelength QWP in one interferometer arm provides the additional delay for one polarization relative to the other. After recombination of the four beams separated by  $\lambda/4$  (two polarizations, two arm lengths plus a QWP in one arm), polarizing beamsplitters sort the combined signals onto four detectors (per wavelength) for sampling of the interferometer fringe (Fig. 1), providing sufficient information to reconstruct both interferometer fringe phase and fringe amplitude.

Except for optical components and electronics, the existing OAWL interferometer structure is all aluminum. Eight individual heater-controller assemblies (with

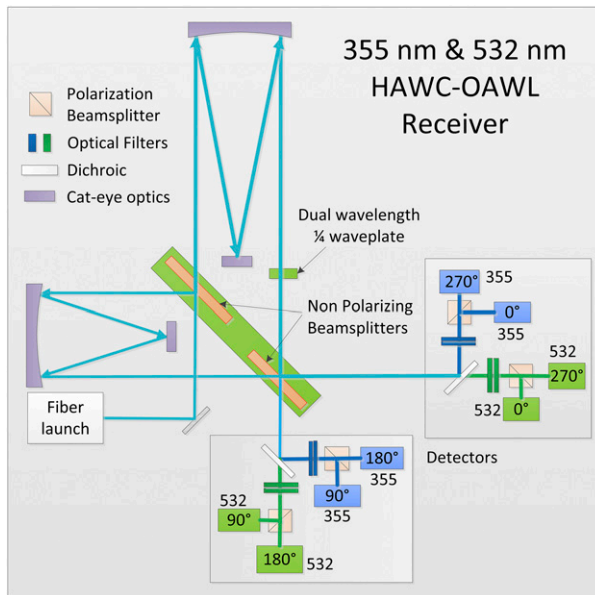


FIG. 5. Cat's-eye field-widened quadrature Mach-Zehnder interferometer receiver block diagram as configured for HAWC-OAWL with four detectors per each of two wavelengths.

controllers, thermistors, and resistive heaters) installed in the interferometer base provide uniform heating of the interferometer arms. These control the temperature of the system at multiple locations to within  $0.1^{\circ}\text{C}$  of the  $35^{\circ}\text{C}$  set point, chosen to ensure active heating control in typical ambient conditions.

#### d. System control

To meet the autonomy levels required for airborne operation on the NASA WB-57, the OAWL systems implement automated operational system software to control the boot sequence, to monitor system performance, to provide user interfaces, to control laser system warm-up and operation processes, and to acquire and store lidar and auxiliary data. To ensure eye safety during aircraft flights and/or ground testing where other aircraft may be near the system (not an issue for space-based orbits), the equipment operators and/or pilots can control when the system lases.

The OAWL-P control and acquisition system consisted of a COTS National Instruments (NI) chassis with a custom field-programmable gate array (FPGA)-based digitizer card, NI data acquisition and communication cards, and an NI controller with custom OAWL-P Labview operations software running on the NI real-time operating system (Table 3).

In contrast, the GrOAWL payload control (PC) subsystem is built to meet high-altitude performance requirements and to ensure all components have a path to space. The chassis is a custom, ruggedized,

conduction-cooled unit with a conduction-cooled single-board computer (SBC) running Linux and two removable solid-state drives for system operation and onboard data storage. The PC contains two auxiliary control boards (ACBs; one per laser/look) that perform triggering (laser pulse detection), laser telemetry digitization and interlock, power and thermal subsystem control (fluid loops, fans, heaters), system timing and GPS synchronization, system telemetry readings, three-axis accelerometer digitization, and trigger/test patterns for system self-testing. The ACBs implement a Xilinx Virtex-5 FPGA to perform processing functions and to interface with the SBC over the chassis bus. A custom backplane overlay board provides uninterrupted pathways for time-critical signals between the ACBs and the data acquisition and processing boards described in the following section.

#### e. Detectors and lidar data acquisition

Table 3 lists the data acquisition parameters for the OAWL systems. All systems to date have used Hamamatsu multipixel photon-counting (MPPC), Geiger-mode, avalanche photodiode arrays mounted to small back-end electronics boards as the detectors. MPPCs have demonstrated improved quantum efficiency with each generation (Yamamoto et al. 2006; Nagano et al. 2012). In the OAWL-P payload controller, custom FPGA-controlled digitizer cards sampled the amplified analog detector signals with 14 bits at a constant 20 MHz (50-ns sample bin).

The all-custom GrOAWL signal chain (see Fig. 6) starts with the small detector electronics boards connected to a custom data acquisition and processing board (APB) that digitally controls, monitors, and samples up to six detectors. When laser triggers are provided by either of the auxiliary control boards (either laser has fired), analog-to-digital converters (ADCs) on the APBs sample all active detector signals at a raw 140-MHz (1.07 m) sample rate, for up to 32 000 samples per channel per pulse. The samples pass to the board's Virtex-5 FPGA, which averages raw samples into longer sample gate bins of variable bin size, reducing the total number of samples to 4096 or less (user defined). During the outgoing time-zero pulse, data are kept at the native 140-MHz sample rate to resolve the pulse shape. For atmospheric returns the FPGA combines samples into bins of varying lengths, from 1 to 32 samples ( $\sim 1\text{--}34\text{ m}$ ) per bin, prior to LOS wind speed processing and storage. Storing the binned instead of raw data enables the system to compress or expand the maximum sample and storage range of the current data system from  $\sim 4$  to  $\sim 34\text{ km}$  based on the desired sample range resolution. Longer ranges are possible if fewer channels, gating, or slower ADC sample rates are used.

TABLE 3. OAWL data acquisition parameters.

Parameters	OAWL-P	GrOAWL	HAWC-OAWL
Payload controller	NI (COTS)	Custom 6U conduction-cooled chassis	
Data system controller	NI controller running NI real-time operating system with Labview	6U conduction-cooled single-board computer running Linux with C++	
System control board	NI COTS	Custom six-channel system control, thermal control and telemetry board, one per laser/look	
Data acquisition board(s)	Custom six-channel ADC boards with VIRTEX-5 FPGA paired with NI COTS FPGA cards for data storage	Custom six-channel ADC board with detector control, data acquisition, and real-time LOS wind speed processing	Two GrOAWL boards, one board per wavelength
Raw-sample range gate (rate)	20 MHz (7.5 m)	140 MHz (1.07 m)	
Binned-sample range gate	7.5 m	Variable accumulation in FPGA: 1.07–34 m	
Sample resolution	14 bit	14-bit raw, 16-bit binned	
Maximum stored samples/pulse/channel	3000	4096	4096
Total lidar data rate (to disk)	4 channels, 200-Hz PRF $\rightarrow$ 4.2 MB s <sup>-1</sup>	4 channels, 400-Hz PRF $\rightarrow$ $\sim$ 13.1 MB s <sup>-1</sup>	10 channels, 400-Hz PRF $\rightarrow$ $\sim$ 32.8 MB s <sup>-1</sup>
Minimum range (overlap limited)	$\sim$ 500 m	$\sim$ 400 m	
Maximum range <sup>a</sup>	Up to 22.5 km	Variable based on binning size, typical data operation up to 34 km	

<sup>a</sup> Limited by data system settings and aerosol-dependent performance.

OAWL wind speed retrieval algorithms, originally developed using MATLAB, were transferred to the APB FPGAs for real-time processing. Once binned, samples are processed in real time into LOS wind speeds with programmable time (number of pulses) and range (number of bins) accumulation values. The APB provides the real-time LOS winds along with raw data to the SBC for storage and/or display. The real-time FPGA wind algorithms were demonstrated during the GrOAWL airborne flight testing as a demonstration for future space-based platform operation, where the LOS wind speed data products may be generated at

the instrument level prior to downlink to minimize latency to weather forecast centers.

The HAWC-OAWL instrument includes the GrOAWL APB for the 532-nm channels, and a second APB for the 355-nm channels, providing acquisition for up to 12 detectors (10 are used). Each APB runs two LOS wind speed processing instantiations simultaneously, one per telescope look, and provides the winds to the payload controller for real-time display and downlink. For the HAWC-OAWL instrument, four LOS wind measurements “curtain” plots (one per look, per wavelength) can be observed simultaneously in real time.

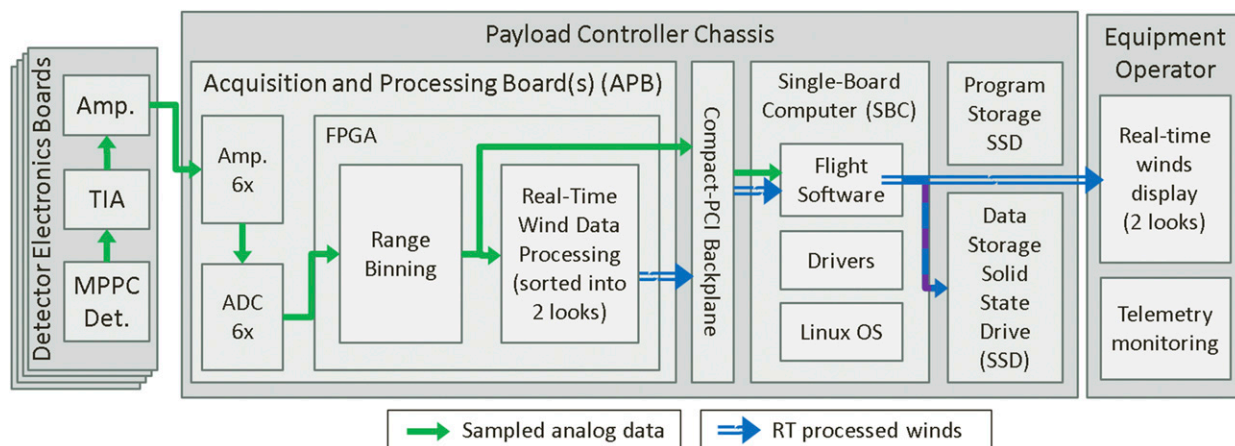


FIG. 6. Data acquisition and real-time processing signal chain for the GrOAWL and HAWC-OAWL instruments. Each APB can handle up to six detector channels, with one board per wavelength. TIA = transimpedance amplifier and Amp = amplifier.

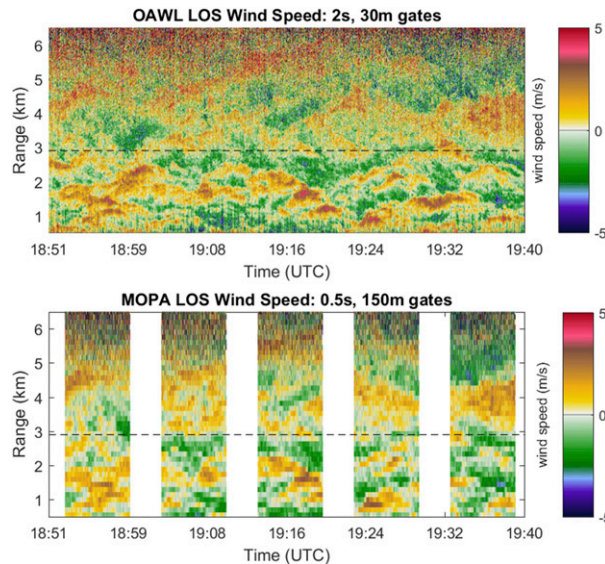


FIG. 7. LOS wind speed data acquired during the 2011 OAWL-P ground-test validation. (top) The 355-nm-wavelength OAWL-P data processed with 30-m range gates and 2-s (400 pulse) accumulation. (bottom) The 9.55- $\mu\text{m}$  NOAA mini-MOPA data processed with 150-m range gates and 0.5-s (150 pulse) accumulation. White gaps in MOPA data indicate times when the system performed scans.

### 3. OAWL testing and validation

The OAWL-P system underwent ground and airborne demonstration and validation testing in summer and fall of 2011. The GrOAWL system likewise had ground testing and airborne flight test demonstration and validation in spring of 2016 (Baidar et al. 2016). These tests and examples of the test results are described here. Full validation results for the GrOAWL system are described in detail in a companion paper (Baidar et al. 2018).

#### a. OAWL-P 2011 ground testing

Ground-based testing alongside the NOAA Earth System Research Laboratory (ESRL) Chemical Science Division's miniature master oscillator power amplifier (mini-MOPA; MOPA) 9.355- $\mu\text{m}$  coherent detection DWL (Pearson et al. 1990; Pearson 1991, 1993; Tucker et al. 2006) provided the initial validation for the OAWL instrument concept. During the tests, from 11 to 21 July 2011, both the MOPA and OAWL systems pointed at 17° [north-northeast (NNE)] azimuth and 0.3° elevation, out over the Department of Commerce's Table Mountain Test Facility, north of Boulder, Colorado, acquiring approximately 15 h of coincident data.

The images in Fig. 7 show a portion of processed LOS wind estimates for data acquired by the two systems on

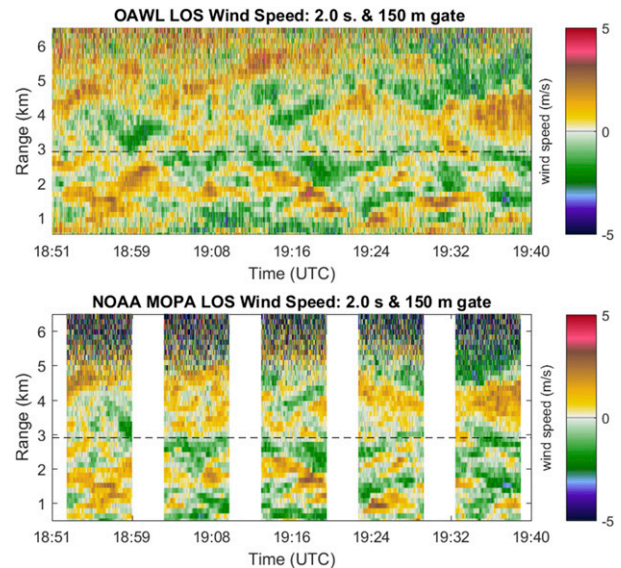


FIG. 8. Data from Fig. 7 interpolated onto the same time-range grid of 2 s and 150 m. MOPA values beyond ~5 km become more negative with averaging because of a nonwhitened noise floor that biases the averages.

13 July 2011. The OAWL data are processed with 30-m range gates and 2 s of accumulation for a total of 1600 samples per estimate. The overlap bias described in section 2c(4) (before fiber coupling the interferometer) was independently estimated using averages over several days of data under varying wind conditions and removed. The NOAA mini-MOPA data (9.35- $\mu\text{m}$  wavelength, 1.5 mJ per pulse, 300-Hz PRF) are processed with 150-m range gates and 0.5 s of accumulation (1500 samples per estimate).

The two datasets were decimated and interpolated (OAWL in range, MOPA in time) to put them on the same 2-s and 150-m time-range grid (Fig. 8). For each 150-m range gate, the correlation coefficients calculated between the time series from each system are plotted versus the range in the top panel of Fig. 9, with a maximum correlation coefficient  $r = 0.92$ , limited by CNR-driven uncertainties for both systems [see Eq. (6); Pearson et al. 1990; Rye and Hardesty 1993]. The bottom panel provides a range-dependent characterization of these system uncertainties (estimated as uncorrelated noise using autocorrelation and fit to zero lag) versus range. The MOPA uncertainty increases very quickly after 4 km, partly because of the lower pulse energy and partly because of the lack of large atmospheric particles, while the OAWL uncertainty increases more slowly with range. Figure 10 contains a scatterplot of all (no thresholding applied) the common-grid OAWL wind speed measurements versus those from MOPA between 0.5 and 4 km, for the period shown in Fig. 7, resulting in a



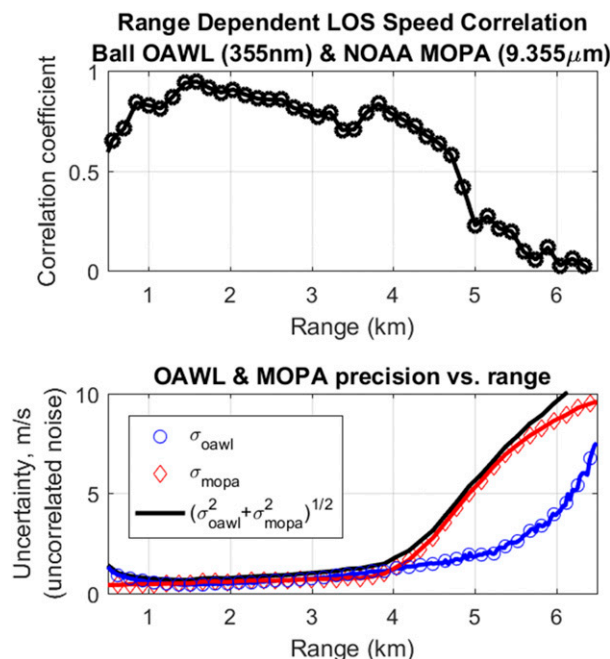


FIG. 9. (top) Range-dependent correlation between the OAWL-P system data and the NOAA mini-MOPA system data after interpolation of both systems onto the same grid. (bottom) Time series-calculated uncorrelated error uncertainty for each system plotted vs range. The root-mean-square of the two instrument uncertainties (black line) is an indicator of how much the uncorrelated noise in each system affects the cross correlation.

linear regression fit with a slope of 0.92 and an offset of  $0.06 \text{ m s}^{-1}$ . Most of the scatter is again due to measurement uncertainty in either system (Fig. 9); however, some scatter is attributed to the separate lines of sight of the two systems. Time-based correlation studies between the two instruments showed that the lag of the peak correlation was sometimes one to two lags or 2–4 s, representing the time that wind cells could take to advect from the LOS of one lidar over to that of the other, which impacts the per-sample differences between the two systems. While differences illustrate spatial offsets, and potential uncertainty and biases are likely present in both systems, the excellent overall agreement illustrates the capability of the direct-detection OAWL to make aerosol wind measurements with precision and accuracy comparable to those from coherent detection lidars like the NOAA MOPA.

#### b. OAWL-P airborne testing

The 2011 OAWL-P flight test objective was to demonstrate the measurement approach looking down as part of a road map to space-based operation. Additional details on the preparation for and implementation of the airborne testing are provided in Tucker et al. (2015). OAWL-P flew 23 flight hours on 5 test flights between

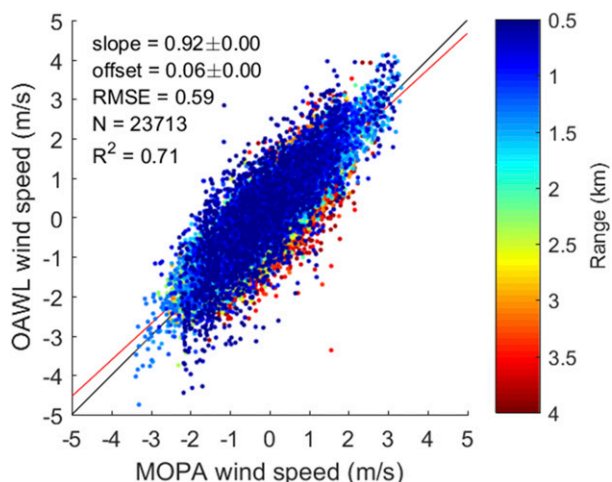


FIG. 10. Scatterplot of OAWL-P LOS-measured wind speed measurements vs those from the NOAA mini-MOPA instrument. Color represents range from the lidars. All measurements between 0.5 and 4 km are shown with no thresholding for either system. The red line shows the best-fit slope of 0.92 and an offset of  $0.06 \text{ m s}^{-1}$ . Black line is 1:1. Standard deviation of all the differences of  $0.59 \text{ m s}^{-1}$  includes uncertainty and/or bias from both instruments.

26 October and 8 November 2011, collecting over 14 h of lidar and auxiliary sensor data.

Program cost caps limited validation to standard aircraft equipment, including aircraft navigation data, to predict expected ground speed, and to operational ground-based systems such as radar wind profilers (RWPs; NOAA ESRL 2017) for atmospheric return. By clockwise-orbiting RWPs, with the OAWL-P system pointing starboard at  $45^\circ$  off nadir (minus aircraft roll angle), the instrument performed “inverse VAD” scans of the atmosphere above the RWP (see Tucker et al. 2015). Limiting the aircraft roll/bank angle to less than  $10^\circ$  as the aircraft orbited the RWP from a flight altitude of approximately 10 km kept the moment arm on horizontal wind vectors to greater than  $35^\circ$ .

Ground returns acquired during cloud-free portions of the flight provided the initial Doppler measurement validation for the OAWL-P flight data. Small offsets to the nominal pointing angle and variations in the aircraft pitch and yaw angles meant that the beam was rarely pointed perfectly perpendicular to the aircraft flight direction, resulting in a nonzero projection of the aircraft speed over ground onto the OAWL-P LOS. Ground returns processed without platform motion correction provide measurements of that projected ground speed and were used to back out the average instrument pointing angle relative to the frame of reference (FoR) of the navigational (NAV) sensor mounted to the aircraft. This angle varied slightly as the aircraft burned fuel, leaving residual speed estimate biases, which led to

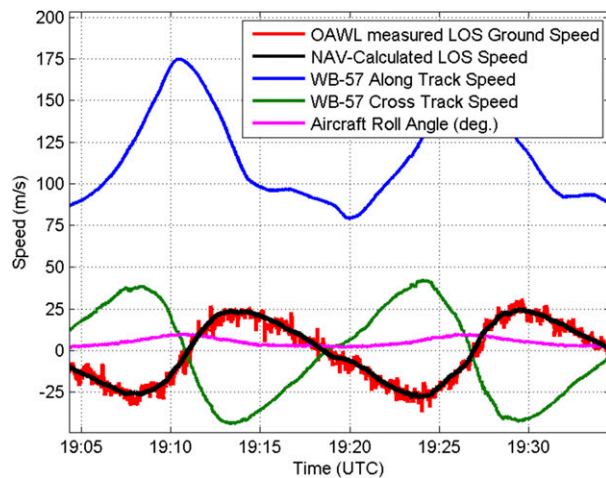


FIG. 11. Airborne OAWL-P-measured LOS ground speed (at  $\sim 11.5$ – $13$ -km range from the aircraft based on aircraft roll and terrain height; red) and the ground speeds predicted by GPS/inertial navigation system data projected onto the OAWL LOS (black).

the installation of a dedicated NAV system directly on the next-generation GrOAWL system. To validate the ground speed measurements, the 1-Hz aircraft NAV data (speed over ground, course over ground, aircraft heading, pitch, and roll) were used to calculate the expected ground speed projected onto the refined OAWL-P LOS pointing angle. Figure 11 contains a plot of the WB-57 NAV data for along-track and cross-track ground speeds (blue and green lines, respectively), and of the ground speed projected onto the OAWL-P LOS pointing angle (black line). The large oscillations in the signal are due to large variations in WB-57 pitch, roll, and yaw angles as it circled a RWP. The red line shows the LOS ground speed as measured by the OAWL instrument, estimated using the single 7.5-m range gate containing the ground return for each pulse and 1-s pulse accumulation. The NAV-calculated and OAWL-P-measured ground speed time series demonstrated an  $R^2$  of 0.96, limited by instrument noise, NAV system averaging, and relative pointing knowledge between the aircraft system and the OAWL-P FOV.

The two ground speed signals, plotted against each other in the scatterplot in Fig. 12, cover a large variation in amplitudes, from approximately  $-29$  to  $+25 \text{ m s}^{-1}$ , demonstrating that the correlation holds up over this entire range. The scatterplot regression revealed a slope of 1.00 with a  $4 \text{ cm s}^{-1}$  offset. The root-mean-square error (difference) between the two signals is approximately  $3.4 \text{ m s}^{-1}$  and includes correlated error from variations in the OAWL-P versus IMU pointing angles and the average precision in these OAWL-P ground return speed estimates,  $\sigma_{v(\text{Ground})}$ , of  $1.8 \text{ m s}^{-1}$  [see section 1b(1)].

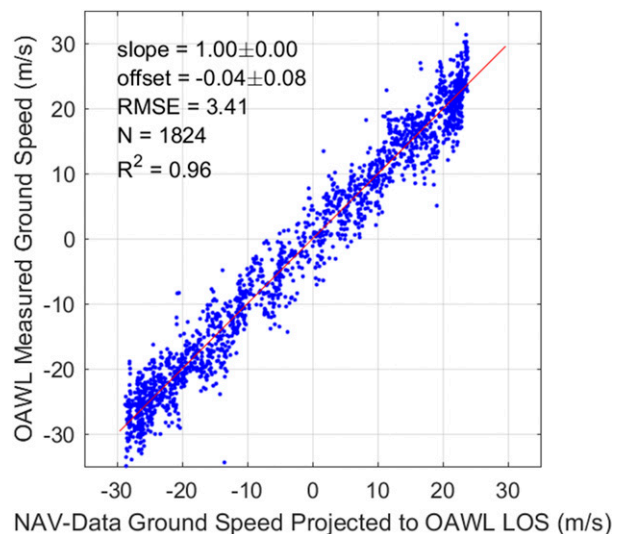


FIG. 12. Scatterplot of OAWL-P-measured ground speed vs NAV data-predicted speed (red vs black lines from Fig. 11).

To validate wind measurements, OAWL-P LOS wind data from the inverse VAD portions of the flight were projected onto the Earth coordinates using interpolated 1-Hz aircraft NAV data and processed into altitude-dependent profiles of wind speed and direction per Browning and Wexler (1968). Figure 13 shows the results of wind speed (left panel) and direction (right panel) profiles plotted versus altitude along with corresponding profiles from the RWP at Marfa, Texas (NOAA ESRL 2017). Two orbits of the aircraft around the profiler took over 30 min, so RWP data within 20 min of the beginning and end times are plotted to demonstrate the wind's variability during the acquisition period.

Differences between the OAWL-P and RWP profiles are due to several factors, including errors on both types of sensor, the low resolution in the aircraft NAV data (and thus in pointing knowledge), differences in the time averages, and large differences in spatial coverage resulting in actual wind variations between the two sampling volumes. The divergence between the two sensors at higher altitudes (closer to the aircraft) is based on the overlap function error described in section 2c(4) and Herbst and Vrancken (2016). As the instrument reaches full overlap (by about 3.5-km altitude), these differences disappear. This issue was eliminated in the GrOAWL system via fiber coupling.

### c. GrOAWL system testing

In contrast to the 355-nm single-look OAWL-P flights, the 2015–17 GrOAWL effort provided an opportunity to build and fly the two-look 532-nm airborne demonstrator system, to validate the measurements using radiosondes, and to verify the OAWL performance.

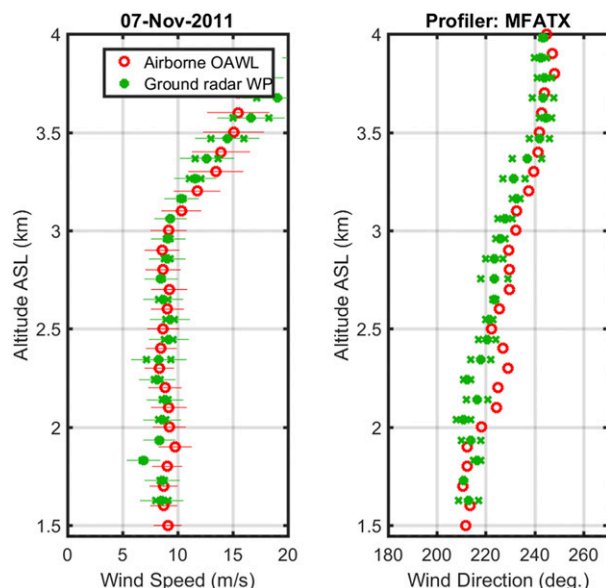


FIG. 13. Airborne OAWL-P wind speed and direction profiles (red circles) acquired from the NASA WB-57 with corresponding radar wind profiler data (green  $\times$  symbols). Measurements above 3.5 km were biased by the instrument overlap function (fixed in later systems using fiber coupling). Surface altitude was variable around 1400 m. Direction uncertainties are unknown.

GrOAWL flight tests included eight flights (a total of 38 flight hours) on the NASA WB-57 in May and June of 2016, over various cloud and aerosol conditions at altitudes ranging from  $\sim 7$  to 15 km. All flights were out of Ellington Field (Houston, Texas). Flight plans included a racetrack pattern in designated aircraft warning areas over the Gulf of Mexico, allowing dropping of radiosondes and providing views of atmospheric volumes from two different sides of the flight track (starboard pointing, clockwise track direction) and revisit times to observe atmospheric variability over the flight duration. Figure 14 (left column) contains images of GrOAWL wind speed data from both looks acquired during the 17 June 2016 flight at 8.5-km altitude. While similar to Fig. 2 in Baidar et al. 2018, data in Fig. 14 were processed with 1-s pulse accumulation (vs. 10 s), demonstrating that additional accumulation generally improves the GrOAWL wind estimate precision. The right column of Fig. 14 shows 10-s processed data from the flight on 21 June 2016. Noisier areas in all images indicate regions of low-aerosol loading. Baidar et al. (2018) contains an additional description of the flight test campaign and results of thorough validation efforts performed using dropsondes and analysis.

#### 4. Impacts on airborne instrument performance

While error analysis for QMZI systems like OAWL is described in Bruneau and Pelon (2003) and a paper

describing the detailed analysis for OAWL is forthcoming, here we discuss specific impacts to GrOAWL instrument performance observed during the 2016 flight tests and subsequent system design modifications for HAWC-OAWL. For a given set of atmospheric scattering conditions, the GrOAWL instrument performance can be broken down into two categories of parameters according to Eq. (5): those that impact instrument throughput efficiency (ITE) and thus lidar SNR, and those that impact instrument contrast (IC) and thus measurement visibility  $V_m$ .

ITE defines the percentage of aerosol plus molecular-backscattered laser photons collected by the telescope that contribute to the total lidar signal, relative to the as-built lidar equation. IC characterizes how well the interferometer resolves Doppler-shifted fringe phases. IC is impacted by the maximum interferometer fringe contrast visibility [Eq. (7)] and by the integrity (precision) of the T0 reference signal. Section 1b(1) and Fig. 1 describe how the per-pulse T0 phases are the reference for all atmospheric returns from that pulse. Uncertainties in T0 phase estimates will therefore impact wind speed retrievals. While derivation of T0 error propagation is left to a later paper, if the T0 signal amplitude is of sufficient SNR ( $>5$ ) and the peak interferometer fringe contrast  $V_{\max}$  is sufficiently high ( $>0.5$ ), then the T0 phase estimate is considered a sufficient reference for the system phase. If the T0 signal amplitude (T0 SNR) is weakened because of thermally induced T0 path misalignments, then the increased T0 phase reference uncertainty will add uncertainty to the wind speed retrievals, even when interferometer contrast is high.

When deployed in the quasi-pressurized pallet ( $\sim 62$  kPa at 9 km) in the WB-57 aircraft pallet bay, both the OAWL-P and GrOAWL instruments faced environmental (thermal, humidity, and vibration) engineering challenges during the flights that were greater than those faced by airborne lidars deployed in temperature-and-pressure-controlled aircraft cabins or on aircraft flying at lower altitudes. These challenges are also often more extreme than known space-flight operational conditions. During the GrOAWL flights (May and June in Houston), the system encountered a wide range of external thermal and relative humidity variations ( $+35^\circ\text{C}$  and  $\sim 90\%$  RH on the tarmac to  $<-35^\circ\text{C}$  and  $\sim 0.1\%$  RH at 10-km altitude). Thus, inside the pallet the instrument operating range and thermal gradients were larger than the design point. Early engineering test flights demonstrated pallet window fogging (reduced ITE), subsequently mitigated by purging humid Houston air out of the sealed pallet with dry nitrogen prior to takeoff and redirecting heater/blower



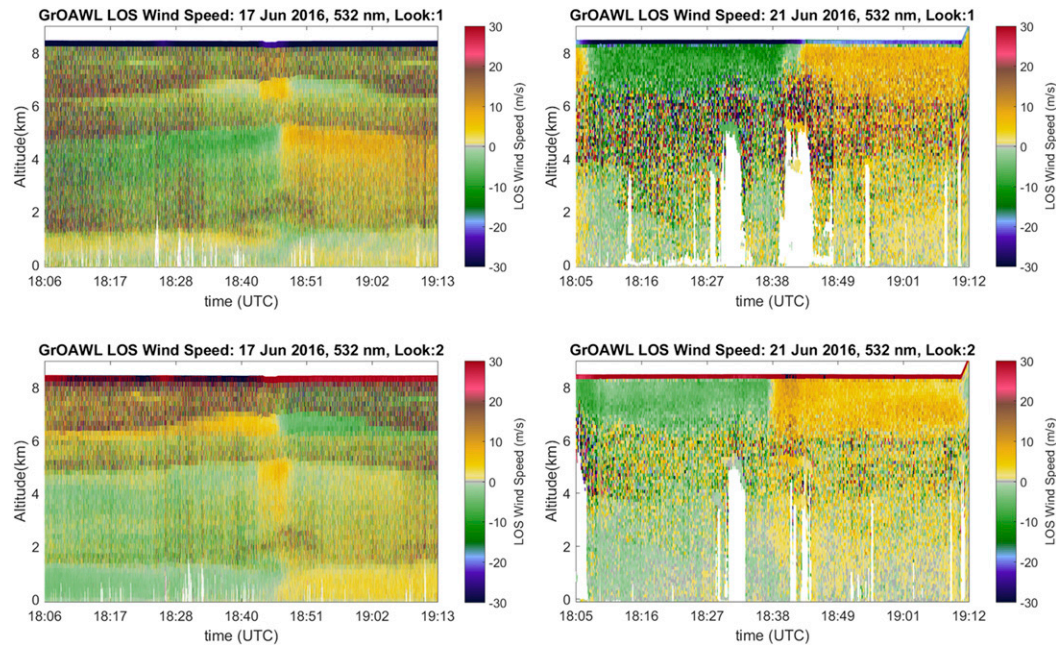


FIG. 14. GrOAWL LOS wind speed flight test data from the NASA WB-57 aircraft at 8.5-km altitude, acquired with  $<0.3$ -W laser power at 532 nm. (top) Look 1 (forward look) and (bottom) look 2 (aft look) data. (left) Data from 17 Jun 2016 processed with 200 pulses (1 s) per profile and 182-m altitude bins. Compare to Fig. 2 in [Baidar et al. \(2018\)](#) with 10-s processing. (right) Data from 21 Jun processed with 2000 pulses (10 s) and 121-m altitude bins. Dark/noisy areas in both images indicate areas of reduced aerosol loading. White areas indicate where returns were completely blocked by clouds.

assemblies over the windows. Over the course of longer flights, strong gradients between the 20° and 30°C pallet interior and the cold exterior and pallet floor caused gradients in the optical bench that reduced ITE via changes in telescope focus and lidar beam overlap. Slow overlap variations (a few minutes or longer) could be adapted to using boresight mechanisms. Thermal gradients also impacted T0 signal alignments (and thus the T0 SNR and thereby the IC). HAWC-OAWL system designs address these issues by updating the telescope flexure mounts (less sensitive to thermal variations) and reducing T0 path alignment sensitivity via overfilling.

The high-vibration environment impacted the GrOAWL performance via small, high rate, telescope misalignments (reduced ITE) that reduced the average SNR. The HAWC-OAWL optomechanical subsystem design used improved integration of optical and mechanical/structural modeling to eliminate these issues by stiffening the telescope flexure mount and optical bench.

Inside the interferometer, a faulty optical mount caused the instrument to be overly sensitive to the high aircraft vibration levels: the optic would vibrate into and out of good alignment positions, thus reducing the overall average measurement precision. The motion also resulted in pulse-to-pulse variations in the interferometer OPD (sometimes up to a few micrometers,

or several wavelengths), which translated into large pulse-to-pulse variations in the T0 reference phase. Per the description surrounding Fig. 1, however, OAWL processing adjusts for all pulse-to-pulse T0 phase variations (arising from variations in interferometer OPD and/or laser frequency) prior to retrieving the LOS winds. On average, these ITE and IC impacts increased GrOAWL airborne wind measurement uncertainty by  $\sim 3.3$  times (see [Baidar et al. 2018](#)). Despite thermal and vibration challenges, the system met the flight objectives and measured accurate winds from multiple flight altitudes ( $\sim 6.5$ – $15$  km), demonstrating precision levels on the order of  $1 \text{ m s}^{-1}$  where sufficient aerosols were present. Lessons learned have been flowed into the next-generation airborne HAWC-OAWL system.

## 5. Ground-based studies and HAWC-OAWL

Before and after the 2016 test flights, ground-based GrOAWL atmospheric testing demonstrated operation of each of the two LOSs from a rooftop laboratory at Ball. The reconfigured HAWC-OAWL system is currently set up in this laboratory to make dual-wavelength wind measurements. The laboratory setup allows for atmospheric returns from only one look at a time. A large mirror placed underneath the optical bench reflects the



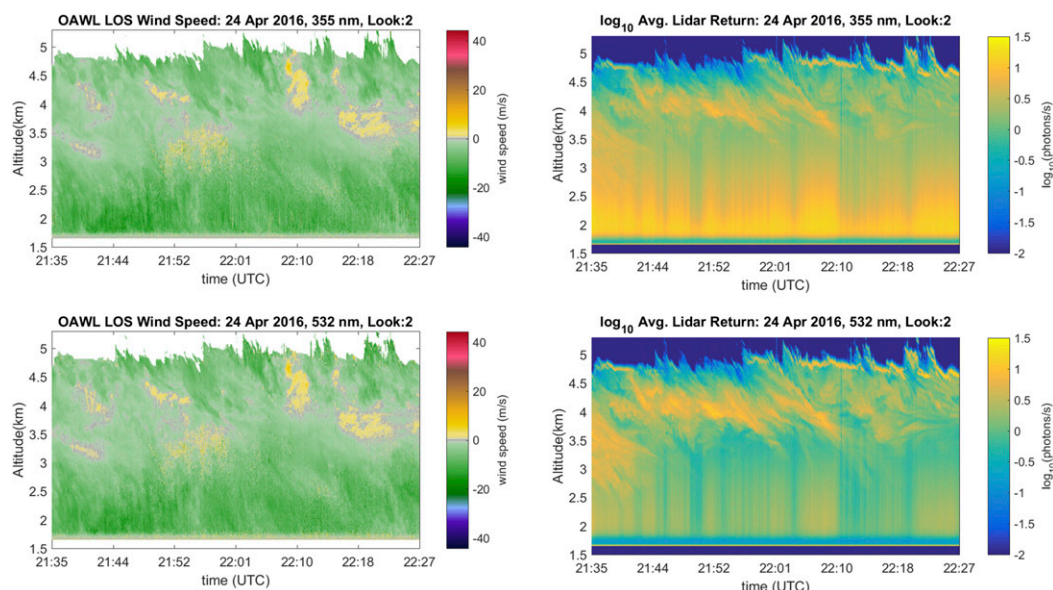


FIG. 15. (left) Ground-based, dual-wavelength, single-LOS wind speed OAWL data taken from the Ball Aerospace rooftop laboratory. (top left) 355-nm-wavelength winds. (bottom left) 532-nm-wavelength winds. (right) Corresponding average lidar returns ( $\log_{10}$  scale) showing the presence of a thick and turbulent convective cloud layer between approximately 3- and 5-km altitude. Vertical striping is attributed to periods when intense near-direct sunlight started to saturate the detector path dynamic range (subsequently increased for HAWC-OAWL to account for additional signal).

beam westward over the Boulder foothills at a  $30^\circ$  elevation angle.

Figure 15 contains ground-test images for both 532-nm ( $\sim 1.25$  mJ per pulse) and 355-nm ( $\sim 11$  mJ per pulse) LOS winds, processed with 2-s (400 pulse) accumulation and 43-m LOS range gates. The LOS data (left panels), acquired on 24 April 2016, show aerosol layers to about 10-km range (5-km altitude) capped by cloud returns. The data show about 2–3 km worth of cloud returns atop a blustery aerosol boundary layer. Performance validation studies for both wavelengths on HAWC-OAWL are currently underway using data acquired concurrently with a nearby high-spectral-resolution lidar.

## 6. Conclusions and next steps

Ball has designed, built, demonstrated, and validated the optical autocovariance wind lidar measurement approach in multiple configurations of the instrument, using the same internally funded QMZI interferometer. The single-look 355-nm OAWL-P system validated the measurement technique with  $<1 \text{ m s}^{-1}$  precision in ground tests with a coherent detection system and in airborne tests using ground returns and ground-based RWP data in 2011. The two-look 532-nm GrOAWL airborne demonstrator system flew in 2016, and LOS wind measurement accuracy was validated using collocated

dropsondes ( $R^2 > 0.9$ ) as discussed in Baidar et al. (2016). Most recently, Ball has completed the build of the HAWC-OAWL system, adding dual-wavelength winds plus cross-polarization measurement capabilities to GrOAWL and reconfiguring the system for future integration on the NASA DC-8. Funding dependent, the next steps for the HAWC system are to (i) develop and validate HSRL product retrievals concurrent with winds for aerosol transport studies, (ii) to perform DC-8 test flights, and (iii) to be available for 355-nm-wavelength calibration/validation of ESA's Aeolus wind lidar mission.

*Acknowledgments.* The authors acknowledge the excellent efforts of the Ball Aerospace OAWL engineering teams, especially Mike Adkins, Jeff Applegate, Rachel Narciso, Robert Pierce, Glen Taudien, Mike Conde, Paul Kaptchen, Tom Bellino, Noah Siegel, Dave Gleeson, Miro Ostaszewski, Tom Delker, Jim Howell, and Christian Grund; and the Fibertek Inc. team, specifically Floyd Hovis and Joe Rudd. Flight tests in 2011 and 2016 were successful thanks to dedicated support from the NASA WB-57 program office engineers, aircraft crew, and pilots. Raul Alvarez and Scott Sandberg of the NOAA Earth System Research Laboratory supported the 2011 ground test with MOPA. Funding for the effort was provided through Ball internal investments and competitive grants managed by the NASA Earth Science Technology Office (ESTO; Parminder Ghuman and

Keith Murray; NNX08AN36G, NNX14AF58G, and NNX15AE57G).

## REFERENCES

- Albert, M., K. Puffenburger, T. Schum, F. Fitzpatrick, S. Litvinovitch, D. Jones, J. Rudd, and F. Hovis, 2016: UV lifetime demonstrator for space-based applications. *Proc. SPIE*, **9879**, 987909, <https://doi.org/10.1117/12.2228371>.
- Atlas, R., and Coauthors, 2015: Observing system simulation experiments (OSSEs) to evaluate the potential impact of an optical autocovariance wind lidar (OAWL) on numerical weather prediction. *J. Atmos. Oceanic Technol.*, **32**, 1593–1613, <https://doi.org/10.1175/JTECH-D-15-0038.1>.
- Baidar, S., S. C. Tucker, and M. Hardesty, 2016: Preliminary results from the ATHENA-OAWL venture tech airborne mission. *Proc. 18th Coherent Laser Radar Conf. and the Lidar Working Group on Space Based Winds (CLRC 2016)*, Boulder, CO, CIRES, F6, <https://clrcires.colorado.edu/clrc2016/4pagesummaries/F/F6.pdf>.
- , —, M. Beaubien, and R. M. Hardesty, 2018: The optical autocovariance wind lidar. Part II: Green OAWL (GrOAWL) airborne performance and validation. *J. Atmos. Oceanic Technol.*, **35**, 2099–2116, <https://doi.org/10.1175/JTECH-D-18-0025.1>.
- Baker, W. E., and Coauthors, 2014: Lidar-measured wind profiles: The missing link in the global observing system. *Bull. Amer. Meteor. Soc.*, **95**, 543–564, <https://doi.org/10.1175/BAMS-D-12-00164.1>.
- Boquet, M., P. Royer, J. Cariou, M. Machta, and M. Valla, 2016: Simulation of Doppler lidar measurement range and data availability. *J. Atmos. Oceanic Technol.*, **33**, 977–987, <https://doi.org/10.1175/JTECH-D-15-0057.1>.
- Browning, K. A., and R. Wexler, 1968: The determination of kinematic properties of a wind field using Doppler radar. *J. Appl. Meteor.*, **7**, 105–113, [https://doi.org/10.1175/1520-0450\(1968\)007<0105:TDOKPO>2.0.CO;2](https://doi.org/10.1175/1520-0450(1968)007<0105:TDOKPO>2.0.CO;2).
- Bruneau, D., 2001: Mach–Zehnder interferometer as a spectral analyzer for molecular Doppler wind lidar. *Appl. Opt.*, **40**, 391–399, <https://doi.org/10.1364/AO.40.000391>.
- , 2002: Fringe-imaging Mach–Zehnder interferometer as a spectral analyzer for molecular Doppler wind lidar. *Appl. Opt.*, **41**, 503–510, <https://doi.org/10.1364/AO.41.000503>.
- , and J. Pelon, 2003: Simultaneous measurements of particle backscattering and extinction coefficients and wind velocity by lidar with a Mach–Zehnder interferometer: Principle of operation and performance assessment. *Appl. Opt.*, **42**, 1101, <https://doi.org/10.1364/AO.42.001101>.
- , A. Garnier, A. Hertzog, and J. Porteneuve, 2004: Wind-velocity lidar measurements by use of a Mach–Zehnder interferometer, comparison with a Fabry–Perot interferometer. *Appl. Opt.*, **43**, 173–182, <https://doi.org/10.1364/AO.43.000173>.
- , F. Blouzon, J. Spatazza, F. Montmessin, J. Pelon, and B. Faure, 2013: Direct-detection wind lidar operating with a multimode laser. *Appl. Opt.*, **52**, 4941–4949, <https://doi.org/10.1364/AO.52.004941>.
- , and Coauthors, 2015: 355-nm high spectral resolution airborne lidar LNG: System description and first results. *Appl. Opt.*, **54**, 8776, <https://doi.org/10.1364/AO.54.008776>.
- Clissold, P., Ed., 2008: ADM-Aeolus science report. ESA Publ. SP-1311, 121 pp., [https://www.esa.int/Our\\_Activities/Observing\\_the\\_Earth/Aeolus/Documents/publications](https://www.esa.int/Our_Activities/Observing_the_Earth/Aeolus/Documents/publications).
- Durand, Y., A. J. Culoma, R. Meynart, D. Morancais, and F. Fabre, 2004: Predevelopment of a direct detection Doppler wind lidar for ADM/AEOLUS mission. *Proc. SPIE*, **5234**, <https://doi.org/10.1117/12.517849>.
- Endemann, M., 2006: ADM-Aeolus: The first spaceborne wind lidar. *Proc. SPIE*, **6409**, 64090G, <https://doi.org/10.1117/12.697081>.
- ESA, 2017: Wind satellite vacuum packed. [https://www.esa.int/Our\\_Activities/Observing\\_the\\_Earth/Aeolus/Wind\\_satellite\\_vacuum\\_packed](https://www.esa.int/Our_Activities/Observing_the_Earth/Aeolus/Wind_satellite_vacuum_packed).
- , 2018: ESA's Aeolus wind satellite launched. [https://www.esa.int/Our\\_Activities/Observing\\_the\\_Earth/Aeolus/ESA\\_s\\_Aeolus\\_wind\\_satellite\\_launched](https://www.esa.int/Our_Activities/Observing_the_Earth/Aeolus/ESA_s_Aeolus_wind_satellite_launched).
- Flesia, C., C. L. Korb, and C. Hirt, 2000: Double-edge molecular measurement of lidar wind profiles at 355 nm. *Opt. Lett.*, **25**, 1466–1468, <https://doi.org/10.1364/OL.25.001466>.
- Goodman, J. W., 1985: *Statistical Optics*. Wiley Series in Pure and Applied Optics, John Wiley & Sons, 500 pp.
- Grund, C. J., and R. M. Pierce, 2009a: Field widening lens. U.S. Patent 7,929,215B1, filed 20 February 2009, and issued 19 April 2011.
- , and —, 2009b: Optical autocovariance lidar. U.S. Patent 8,077,294B1, filed 21 January 2009, and issued 13 December 2011.
- , and S. C. Tucker, 2011: Optical Autocovariance Wind Lidar (OAWL): A new approach to direct detection Doppler wind profiling. *Fifth Symp. on Lidar Atmospheric Applications*, Seattle, WA, Amer. Meteor. Soc., 4.9, <https://ams.confex.com/ams/91Annual/webprogram/Paper188184.html>.
- , M. Lieber, B. Pierce, M. Stephens, and C. Weimer, 2008: Optical Autocovariance Wind Lidar (OAWL) for efficient space-based direct detection high-resolution aerosol backscatter winds. *24th International Laser Radar Conference 2008 (ILRC 24)*, Vol. 1, ICLAS, 60–63.
- , J. Howell, R. Pierce, and M. Stephens, 2009: Optical autocovariance direct detection lidar for simultaneous wind, aerosol, and chemistry profiling from ground, air, and space platforms. *Proc. SPIE*, **7312**, 73120U, <https://doi.org/10.1117/12.832721>.
- Herbst, J., and P. Vrancken, 2016: Design of a monolithic Michelson interferometer for fringe imaging in a near-field, UV, direct-detection Doppler wind lidar. *Appl. Opt.*, **55**, 6910–6929, <https://doi.org/10.1364/AO.55.006910>.
- Hill, R. J., W. A. Brewer, and S. C. Tucker, 2008: Platform-motion correction of velocity measured by Doppler lidar. *J. Atmos. Oceanic Technol.*, **25**, 1369–1382, <https://doi.org/10.1175/2007JTECHA972.1>.
- Hovis, F. E., J. Edelman, T. Schum, J. Rudd, and K. Andes, 2008: Recent progress on single frequency lasers for space and high altitude aircraft applications. *Proc. SPIE*, **6871**, 68710E, <https://doi.org/10.1117/12.768278>.
- Hunt, W. H., M. A. Vaughan, K. A. Powell, and C. Weimer, 2009: CALIPSO lidar description and performance assessment. *J. Atmos. Oceanic Technol.*, **26**, 1214–1228, <https://doi.org/10.1175/2009JTECHA1223.1>.
- Kay, S. M., 1993: *Fundamentals of Statistical Signal Processing: Estimation Theory*, Vol. 1, Prentice-Hall Signal Processing Series, Prentice Hall, 595 pp.
- Korb, C. L., B. M. Gentry, and S. X. Li, 1997: Edge technique Doppler lidar wind measurements with high vertical resolution. *Appl. Opt.*, **36**, 5976–5983, <https://doi.org/10.1364/AO.36.005976>.
- Le Rille, O., M. Endemann, A. Culoma, and D. Wernham, 2012: ADM-Aeolus: ESA's high spectral resolution Doppler wind lidar mission, recent achievements and future prospects. *Proc. 26th Int. Laser Radar Conf. (ILRC 26)*, Porto Heli, Greece, ICLAS, S50-01.

- Liu, Z., and T. Kobayashi, 1996: Differential discrimination technique for incoherent Doppler lidar to measure atmospheric wind and backscatter ratio. *Opt. Rev.*, **3**, 47–52, <https://doi.org/10.1007/s10043-996-0047-0>.
- Lux, O., C. Lemmerz, F. Weiler, U. Marksteiner, B. Witschas, S. Rahm, A. Schäfer, and O. Reitebuch, 2018: Airborne wind lidar observations over the North Atlantic in 2016 for the pre-launch validation of the satellite mission Aeolus. *Atmos. Meas. Tech.*, **11**, 3297–3322, <https://doi.org/10.5194/amt-11-3297-2018>.
- Ma, Z., L. P. Riishøjgaard, M. Masutani, J. S. Woollen, and G. D. Emmitt, 2015: Impact of different satellite wind lidar telescope configurations on NCEP GFS forecast skill in observing system simulation experiments. *J. Atmos. Oceanic Technol.*, **32**, 478–495, <https://doi.org/10.1175/JTECH-D-14-00057.1>.
- Marksteiner, U., O. Reitebuch, S. Rahm, I. Nikolaus, C. Lemmerz, and B. Witschas, 2011: Airborne direct-detection and coherent wind lidar measurements along the east coast of Greenland in 2009 supporting ESA's Aeolus mission. *Proc. SPIE*, **8182**, 81820J, <https://doi.org/10.1117/12.897528>.
- Marseille, G.-J., A. Stoffelen, and J. Barkmeijer, 2008: Impact assessment of prospective spaceborne Doppler wind lidar observation scenarios. *Tellus*, **60A**, 234–248, <https://doi.org/10.1111/j.1600-0870.2007.00289.x>.
- Nagano, T., K. Yamamoto, K. Sato, N. Hosokawa, A. Ishida, and T. Baba, 2012: Improvement of Multi-Pixel Photon Counter (MPPC). *2011 IEEE Nuclear Science Symposium Conference Board*, IEEE, 1657–1659, <https://doi.org/10.1109/NSSMIC.2011.6154655>.
- NASA, 2007: NASA systems engineering handbook. Rev1, NASA Publ. NASA/SP-2007-6105, 340 pp.
- NOAA ESRL, 2017: Physical Sciences Division data search. <https://www.esrl.noaa.gov/psd/data/obs/datadisplay/>.
- Paffrath, U., C. Lemmerz, O. Reitebuch, B. Witschas, I. Nikolaus, and V. Freudenthaler, 2009: The airborne demonstrator for the direct-detection Doppler wind lidar ALADIN on ADM-Aeolus. Part II: Simulations and Rayleigh receiver radiometric performance. *J. Atmos. Oceanic Technol.*, **26**, 2516–2530, <https://doi.org/10.1175/2009JTECHA1314.1>.
- Pearson, G. N., 1991: Design and performance characteristics of a compact CO<sub>2</sub> Doppler lidar transmitter. *Proc. SPIE*, **1416**, <https://doi.org/10.1117/12.43720>.
- , 1993: A high-pulse-repetition-frequency CO<sub>2</sub> Doppler lidar for atmospheric monitoring. *Rev. Sci. Instrum.*, **64**, 1155–1157, <https://doi.org/10.1063/1.1144110>.
- , B. J. Rye, and R. M. Hardesty, 1990: Design of a high pulse repetition rate CO<sub>2</sub> Doppler lidar for atmospheric monitoring. *Proc. SPIE*, **1222**, <https://doi.org/10.1117/12.18380>.
- Reitebuch, O., 2012: Wind lidar for atmospheric research. *Atmospheric Physics: Background, Methods, Trends*, U. Schumann, Ed., Research Topics in Aerospace, Springer, 487–507, [https://doi.org/10.1007/978-3-642-30183-4\\_30](https://doi.org/10.1007/978-3-642-30183-4_30).
- , C. Lemmerz, N. Engelbert, and U. Paffrath, 2009: The airborne demonstrator for the direct-detection Doppler wind lidar ALADIN on ADM-Aeolus. Part I: Instrument design and comparison to satellite instrument. *J. Atmos. Oceanic Technol.*, **26**, 2501–2515, <https://doi.org/10.1175/2009JTECHA1309.1>.
- Rye, B. J., and R. M. Hardesty, 1993: Discrete spectral peak estimation in Doppler lidar. I: Incoherent spectral accumulation and the Cramer–Rao bound. *IEEE Trans. Geosci. Remote Sens.*, **31**, 16–27, <https://doi.org/10.1109/36.210440>.
- Schwemmer, G. K., D. O. Miller, T. D. Wilkerson, I. Andrus, and D. V. Guerra, 2001: Large aperture scanning lidar based on holographic optical elements. *IGARSS 2001: 2001 IEEE International Geoscience and Remote Sensing Proceedings*, Vol. 7, IEEE, 3129–3131, <https://doi.org/10.1109/IGARSS.2001.978279>.
- , R. D. Rallison, T. D. Wilkerson, and D. V. Guerra, 2006: Holographic optical elements as scanning lidar telescopes. *Opt. Lasers Eng.*, **44**, 881–902, <https://doi.org/10.1016/j.optlaseng.2005.06.011>.
- Schwiesow, R. L., and L. Lading, 1981: Temperature profiling by Rayleigh-scattering lidar. *Appl. Opt.*, **20**, 1972–1979, <https://doi.org/10.1364/AO.20.001972>.
- , and S. D. Mayor, 1995: Coherent optical signal processing for a Doppler lidar using a Michelson interferometer. *Coherent Laser Radar: Summaries of the Papers Presented at the Topical Meeting*, OSA Technical Digest Series, Vol. 19, Optical Society of America, 212–215.
- Stoffelen, A., G. J. Marseille, F. Bouttier, D. Vasiljevic, S. de Haan, and C. Cardinali, 2006: ADM-Aeolus Doppler wind lidar Observing System Simulation Experiment. *Quart. J. Roy. Meteor. Soc.*, **132**, 1927–1947, <https://doi.org/10.1256/qj.05.83>.
- Straume, A. G., and Coauthors, 2016: ESA's spaceborne lidar mission ADM-Aeolus; recent achievements and preparations for launch. *EPJ Web Conf.*, **119**, 01001, <https://doi.org/10.1051/epjconf/201611901001>.
- Tucker, S. C., W. Brewer, M. J. Post, A. M. Weickmann, C. J. Senff, and R. M. Hardesty, 2006: Doppler lidar measurements of wind and velocity turbulence profiles in the Mount Washington Valley, October 2003. *Proc. Seventh Int. Symp. on Tropospheric Profiling*, Boulder, CO, NCAR and NOAA, 7.13-P.
- , and Coauthors, 2015: Optical autocovariance wind lidar (OAWL): Aircraft test-flight history and current plans. *Proc. SPIE*, **9612**, 96120E, <https://doi.org/10.1117/12.2190792>.
- , R. M. Hardesty, S. Baidar, and C. Weimer, 2016a: The ATHENA-OAWL venture tech instrument. *Proc. 18th Coherent Laser Radar Conf. and the Lidar Working Group on Space Based Winds (CLRC 2016)*, Boulder, CO, CIRES, F5, <https://clrcires.colorado.edu/clrc2016/4pagesumaries/F/F5.pdf>.
- , C. Weimer, and R. M. Hardesty, 2016b: The ATHENA-OAWL Doppler wind lidar mission. *EPJ Web Conf.*, **119**, 01002, <https://doi.org/10.1051/epjconf/201611901002>.
- Wang, S., G. G. Shepherd, and W. E. Ward, 2000: Optimized reflective wide-angle Michelson phase-stepping interferometer. *Appl. Opt.*, **39**, 5147–5160, <https://doi.org/10.1364/AO.39.005147>.
- Weimer, C., S. Tucker, W. Baker, R. M. Hardesty, and L. P. Riishøjgaard, 2015: The ATHENA-OAWL Doppler wind lidar mission. *Fifth Conf. on Transition of Research to Operations*, Phoenix, AZ, Amer. Meteor. Soc., J4.4, <https://ams.confex.com/ams/95Annual/webprogram/Paper268581.html>.
- Winker, D. M., M. A. Vaughan, A. Omar, Y. Hu, K. A. Powell, Z. Liu, W. H. Hunt, and S. A. Young, 2009: Overview of the CALIPSO mission and CALIOP data processing algorithms. *J. Atmos. Oceanic Technol.*, **26**, 2310–2323, <https://doi.org/10.1175/2009JTECHA1281.1>.
- Yamamoto, K., K. Yamamura, K. Sato, T. Ota, H. Suzuki, and S. Ohsuka, 2006: Development of Multi-Pixel Photon Counter (MPPC). *2006 IEEE Nuclear Science Symposium Conference Record*, B. Philips, Ed., Vol. 2, IEEE, 1094–1097, <https://doi.org/10.1109/NSSMIC.2006.356038>.